
This copy is for your personal, non-commercial use only.

If you wish to distribute this article to others, you can order high-quality copies for your colleagues, clients, or customers by [clicking here](#).

Permission to republish or repurpose articles or portions of articles can be obtained by following the guidelines [here](#).

The following resources related to this article are available online at www.sciencemag.org (this information is current as of October 23, 2014):

Updated information and services, including high-resolution figures, can be found in the online version of this article at:

<http://www.sciencemag.org/content/345/6199/916.full.html>

Supporting Online Material can be found at:

<http://www.sciencemag.org/content/suppl/2014/08/20/345.6199.916.DC1.html>

This article **cites 30 articles**, 8 of which can be accessed free:

<http://www.sciencemag.org/content/345/6199/916.full.html#ref-list-1>

This article appears in the following **subject collections**:

Materials Science

http://www.sciencemag.org/cgi/collection/mat_sci

NANOPARTICLE GROWTH

Facet development during platinum nanocube growth

Hong-Gang Liao,¹ Danylo Zherebetsky,¹ Huolin Xin,¹ Cory Czarnik,² Peter Ercius,³ Hans Elmlund,⁴ Ming Pan,² Lin-Wang Wang,¹ Haimei Zheng^{1,5*}

An understanding of how facets of a nanocrystal develop is critical for controlling nanocrystal shape and designing novel functional materials. However, the atomic pathways of nanocrystal facet development are mostly unknown because of the lack of direct observation. We report the imaging of platinum nanocube growth in a liquid cell using transmission electron microscopy with high spatial and temporal resolution. The growth rates of all low index facets are similar until the {100} facets stop growth. The continuous growth of the rest facets leads to a nanocube. Our calculation shows that the much lower ligand mobility on the {100} facets is responsible for the arresting of {100} growing facets. These findings shed light on nanocrystal shape-control mechanisms and future design of nanomaterials.

Important advances have been made in synthesis of nanocrystals with a variety of shapes—including cube, cuboctahedron, octahedron, tetrahedron, decahedron, icosahedron, thin plate, and rod—strongly influencing performance in catalysis, sensing, and many other surface-enhanced applications (1–6). The Wulff construction has been used to predict the equilibrium shape of nanocrystals (7, 8), where it states that the length of a normal vector drawn from the crystal center to an external surface is proportional to the surface free energy. This model can be traced back to 1873, when Gibbs proposed that the equilibrium shape of a droplet of matter is determined by a surface energy minimization (9, 10). In the growth of nanocrystals, the high-energy facet grows at a higher rate than the low-energy facets; therefore, the fast-growing facets will eventually disappear, resulting in a nanocrystal terminated with low-energy facets (11–13). It is assumed that the commonly used surfactants modify the energy of specific facets through preferential adsorption, influencing the relative growth rate of different facets and thus the shape of a nanocrystal (8, 14). However, the existing models are based on postreaction characterizations. The evolving facet dynamics during nanocrystal growth is largely unknown.

Microfabricated liquid cells allow for in situ observation of single-nanoparticle growth trajectories using transmission electron microscopy (TEM) (15–18). A liquid cell encapsulates and maintains a small amount of liquid inside the high-vacuum microscope for an extended period of time. Nanocrystal growth can be initiated by thermal heating or, more commonly, by elec-

tron beam irradiation. Nanocrystals that resemble those in flask synthesis have been created in a liquid cell and imaged with TEM (19–21). However, it is a challenge to image the facet development at the atomic level because of the limited signal-to-noise ratio of the detector, especially when the particle is small and moving dynamically in the field of view. In addition, nanoparticles with well-defined shapes—such as cubes, tetrahedrons, and so on—are hard to achieve when there is frequent coalescence during growth or when the time for reaction in the

cell is limited. We studied the growth of platinum nanocubes in a liquid cell under TEM by incorporating an advanced high-resolution fast-detection camera (K2-IS camera from Gatan, Incorporated). The K2-IS camera captures electron images directly on a CMOS (complimentary metal-oxide semiconductor) sensor at 400 fps (frames per second) with 2000 pixel by 2000 pixel resolution. The camera can also be configured to capture images at up to 1600 fps with appropriate scaling of the field of view. The elimination of the traditional scintillation process during image detection results in significant improvement in both sensitivity and image resolution. The thin silicon nitride membrane of the liquid cell window (about 10 nm thick for each membrane) facilitates the high-resolution imaging.

The growth solution was prepared by dissolving Pt(acetylacetonate)₂ (20 mg/ml) in a solvent mixture of oleylamine, oleic acid, and pentadecane (4.5:1.5:4). About 50 nl of growth solution were loaded into one of the reservoirs in a liquid cell. The solution was drawn into the cell by capillary force and formed a liquid layer (100 nm) sandwiched between two silicon nitride membranes at the window. We filled the other reservoir with the growth solution. The liquid precursor solution was well sealed inside the cell, allowing an extended period of time for reaction. A FEI Tecnai F20 TEM (200 kV, FEI, Hillsboro, OR) equipped with the K2-IS camera was used, and a beam current density of $4.0 \pm 0.9 \times 10^5$ A/m² was maintained during movie acquisition.

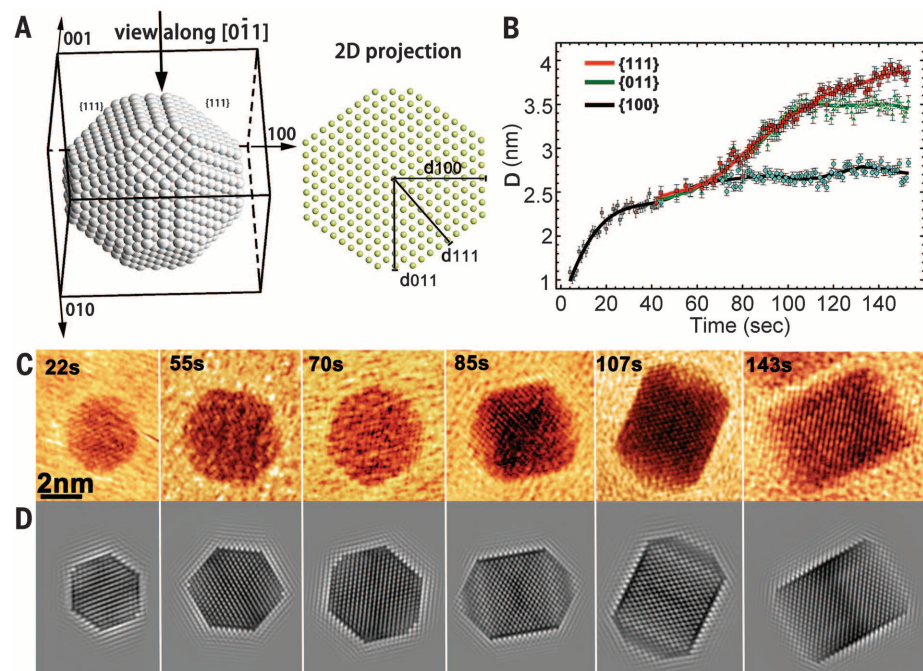


Fig. 1. The facet development of a Pt nanocube viewed along the $[0\bar{1}1]$ axis. **(A)** The atomic model of a truncated Pt nanocube and its projection along the $[0\bar{1}1]$ view zone axis. The distances from the crystal center to each of the (100), (011), and (111) facets are highlighted. **(B)** The measured average distances from the crystal center to each facet as a function of time. Error bars indicate the standard deviation. **(C)** Sequential images show the growth of the Pt nanocube extracted from movie S2. **(D)** Simulated TEM images of the Pt nanoparticle in (C).

¹Materials Sciences Division, Lawrence Berkeley National Laboratory, Berkeley, CA 94720, USA. ²Gatan, Incorporated, 5794 West Las Positas Boulevard, Pleasanton, CA 94588, USA. ³National Center for Electron Microscopy, Lawrence Berkeley National Laboratory, Berkeley, CA 94720, USA. ⁴Department of Structural Biology, Medical School, Stanford University, Stanford, CA 94305, USA. ⁵Department of Material Science and Engineering, University of California, Berkeley, CA 94720, USA.

*Corresponding author. E-mail: hmzheng@lbl.gov

The nucleation and growth of platinum nanocrystals is initiated by irradiating the precursor solution with the electron beam. A burst of nucleation is observed at the beginning while the sample is focused for imaging. Subsequently, more nanoparticles appear. Although there are some coalescence events of nanoparticles in the early stage of growth, most nanoparticles eventually develop into nanocubes by the attachment of monomeric species (movie S1). Nanoparticles frequently rotate during the early stage of growth and become more stationary, sitting on a certain facet, during the later development.

We quantified the shape evolution of a Pt nanoparticle by tracking the propagation of different facets. Figure 1 shows a nanoparticle primarily registered along the [110] viewing axis during facet development, which allowed measurements of the distance from the center of crystal to all three facets: {100}, {110}, and {111} (see the three-dimensional model and two-dimensional projection in Fig. 1A). Movie S2 shows the growth trajectory of the nanoparticle: It rotates as a small and round nanoparticle at the early stage, and it sits along the [110] viewing axis while occasionally rocking off-axis as it becomes faceted (see the movie processing in the supplementary materials). Changes in the distance from the center of crystal to each facet as a function of time are plotted in Fig. 1B. Sequential TEM images

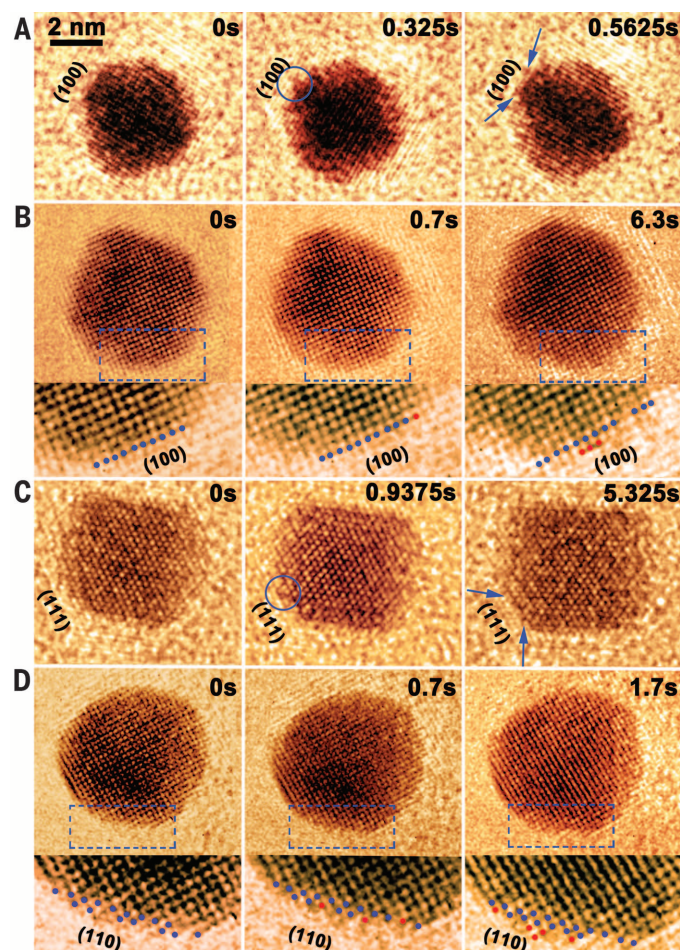
extracted from movie S2 are displayed in Fig. 1C. At the early stage of growth (0 to 70 s), although the three low-energy facets ({100}, {110}, and {111}) are identifiable, the particle appears to be almost round and rotates frequently. The particle grows while maintaining the truncated octahedron shape; therefore, all three facets have a similar growth rate. When the distance from the center of crystal to the surface of {100} facets reaches about 2.5 nm, growth of these facets stops. During the subsequent period of time (70 to 100 s), both {110} and {111} facets continue to grow with a similar growth rate until the {110} facets reach the limiting point defined by the two neighboring {100} facets. Last, only the {111} facets grow, which is shown as the surface area of each {111} facet becoming smaller and the corners of a cube being filled. Because each {111} facet is confined by three neighboring {100} facets, eventually the {111} facets disappear when the nanoparticle becomes a cube. During these facet developments, the nanoparticle mostly stays along the [110] axis with occasional rocking off-axis. To identify the off-axis angle of the nanoparticle in each image, we simulated collages of images with 5°-by-5° off-axis and selected the best matches from the collage by visual comparison (figs. S10 to S20). As confirmed by the simulated images in Fig. 1D, the nanoparticle is only a few degrees off-axis.

We found that most of the nanoparticles follow the above growth model, where all three low-index facets grow with a similar rate and the shape of the nanoparticle is determined when the {100} facets cease growth. Such a selective facet-arrested shape-control mechanism deviates from what is predicted by the surface energy minimization theories. The similar growth rate of different facets is probably due to the fact that almost all the atoms are near the surface for such small nanocrystals, so atoms can rearrange easily (21). The differences in the nucleation barrier on various facets can be very small.

Tracking the nanocrystal growth trajectories reveals the atomic development of different facets. Figure 2 shows the attachment of atoms or clusters to the {100}, {110}, and {111} facets during growth (see image analysis in the supplementary materials and fig. S3). On both the {100} and the {111} facets, it is observed that small clusters of atoms directly attach to the facet. The subsequent addition of atoms leads to the layer-by-layer growth of the facet (Fig. 2, A to C). During the growth of nanoparticles, most of the time we observed the flat propagation of {100} and {111} facets. This implies that, once there is a nucleation event on the flat facet, the lateral growth of the atomic layer can be very fast. Nucleation should be the controlling step of these facets' development. However, the {110} facets grew with steps, and a nonflat surface was observed (Fig. 2D). Apparently, surfactant ligands do not block the attachment of atoms to the nanoparticle surface during the early stage of growth. It has also been observed that some atoms disappeared on certain facets, suggesting that dissociation or rearrangement of atoms may occur. Atoms directly knocked off by electron beam cannot be excluded. Delocalization resulting from spherical aberration produces images with nonsharp edges. However, because we recorded a series of images with high signal-to-noise ratio and with high temporal resolution (2.5 ms per frame), the atomic growth pathways are identified without ambiguity by comparing images frame by frame.

Observations also show that the facet growth rate of nanoparticles fluctuates. As an example, Fig. 3 shows the growth trajectories of a nanoparticle mostly in the [100] viewing direction (movie S3). The growth kinetics of four different {110} facets can be measured (Fig. 3A). The distance from the center of crystal to the edge of each facet—(110), ($\bar{1}\bar{1}0$), ($1\bar{1}0$) and ($\bar{1}10$)—as a function of time is plotted in Fig. 3B. There is a similar growth rate among different facets before the {100} facets' growth halt (fig. S2). However, the subsequent growth of the four {110} facets varies. Figure 3C illustrates that the (110) facet grows slower than the other ($\bar{1}\bar{1}0$), ($1\bar{1}0$), and ($\bar{1}10$) facets. As a result, asymmetric nanoparticles with missing corners were observed in the projected images (also see the simulated images in Fig. 3D). However, the slow-growing (110) facet can catch up eventually, completing a symmetric cubic nanocrystal. These growth fluctuations may arise from the local environmental variations, such as impurity molecules, inhomogeneous

Fig. 2. Snapshots of high-resolution images show the atomic facet development. (A) The attachment of a cluster to the (100) facet. (B) The atomic layer attachment to the (100) facet and nucleation on flat (100) facet. (C) The atomic layer attachment to the (111) facet. (D) The atomic growth of the (110) facet shows steps. The circles highlight atoms attaching to the (100) and the (111) facets. Arrows show the atomic layer propagation after nucleation. The red dots show the newly added Pt atoms.



absorption of surfactants, reactant concentration alternation, or the fundamental random nature of atom addition to such small nanoparticles. We have also observed one atomic layer difference of facet-to-facet distances between {100} facets in some nanoparticles, reflecting the growth fluctuations.

A critical question arises: Why do the {100} facets stop growing sooner than the other facets? We calculated the surface energies and binding energies of the ligands on {111} versus {100} facets by using ab initio density functional theory. The amine group of the oleylamine molecule functionalizes the Pt atoms on the surface. Therefore, we simplified the calculations by truncating the long oleyl ($-C_{18}H_{35}$) chain to the ethyl ($-C_2H_5$) group (see more details in the supplementary materials). We skipped the {110} facets because {110} facets can be considered as an intermediate surface between {111} and {100} surfaces, where a {110} facet can be built with a {111} subfacet and a {001} subfacet or two {100} subfacets. In addition, we have observed that the {110} facets are not flat (Fig. 2), so the surfactant binding to a {110} facet is complex. The unpassivated surface energies for the {100} and {111} facets are 10.33 and 7.68 eV/nm² respectively. The maximum surface binding energies are calculated to be -3.19 eV/nm² (0.74 eV per molecule) and -2.19 eV/nm² (0.58 eV per molecule) for {100} and {111} facets. Thus, after taking into account the ligand binding energy, the surface energy with ligand passivation is 7.14 eV/nm² for the {100} facets and 5.49 eV/nm² for the {111} facets. These surface energies do not yield a cubic shape according to the Wulff construction. This further confirms that the final shape of the nanocrystal is not determined by thermodynamic equilibrium; rather, it is determined by growth kinetics. Several factors could play an important role to distinguish the {100} from the {111} facets, including the ability to remove one ligand molecule from the surface, the packing density, and the mobility of the ligand molecules on the surface (see more detailed discussions in the supplementary materials). Considering that growth on both {100} and {111} facets starts from the center of the facet (Fig. 2), the surface ligands must make room for platinum to land on the facet. There are different mechanisms to block this process. The calculated ligand packing densities on {100} and {111} facets are about 0.23-nm² and 0.26-nm² area per ligand molecule, respectively. This small difference in packing density should not differentiate the growth of {100} facets from {111} facets because of the variations in ligand packing resulting from ligand bending, tilting, etc. The calculated energy barriers for a molecule to move from one site to a nearby site are 0.298 and 0.545 eV on the individual {111} and {100} facets, which are smaller than the ligand-surface binding energies of 0.74 and 0.58 eV per molecule on the {100} and {111} facets. (Fig. 4; see details of the calculation in the supplementary materials). Therefore, it is energetically favorable for one ligand molecule to jump from one site to another site on the surface rather than removing

from the surface. The hopping time of one ligand from one site to another can be estimated by using

$$t = t_0 e^{E_{\text{barrier}}/k_B T}$$

where t_0 is a phonon vibrational period that is typically 1 ps, E_{barrier} is the calculated hopping energy barrier, k_B is the Boltzmann constant, and T is the room temperature. The resulting hopping time is about 10^{-6} s on the {111} facet

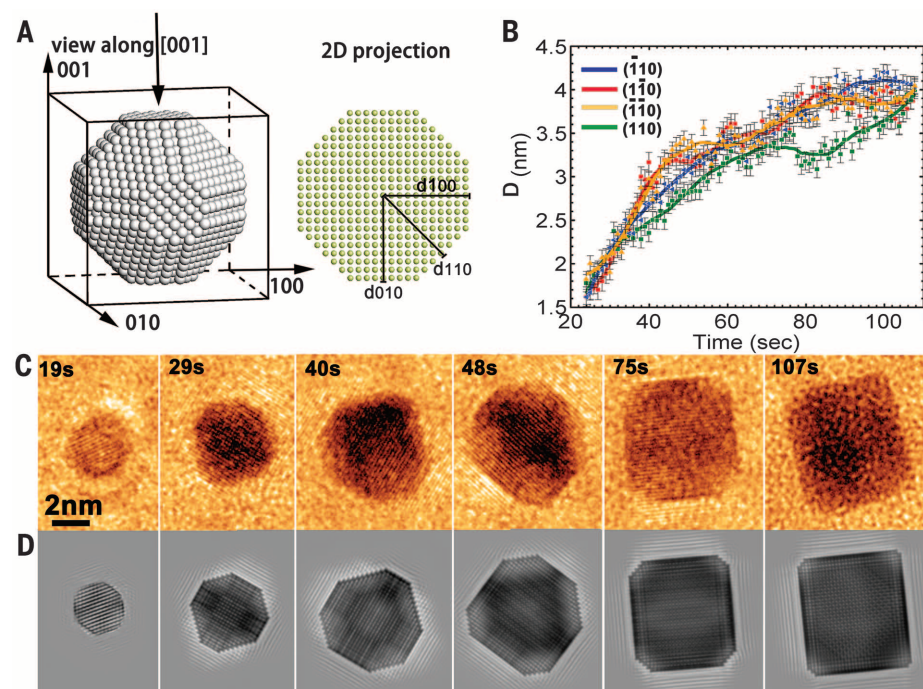


Fig. 3. The facet development of a Pt nanocube viewed along the [001] axis. (A) The atomic model of a truncated Pt nanoparticle and its projection along the [001] view zone axis. **(B)** The measured distances from the crystal center to each of the $(\bar{1}10)$, $(1\bar{1}0)$, $(\bar{1}\bar{1}0)$, and (110) facets as a function of time. Error bars indicate the standard deviation. **(C)** Sequential images show the growth of the Pt nanocube extracted from movie S3. **(D)** Simulated TEM images of the Pt nanoparticle in (C).

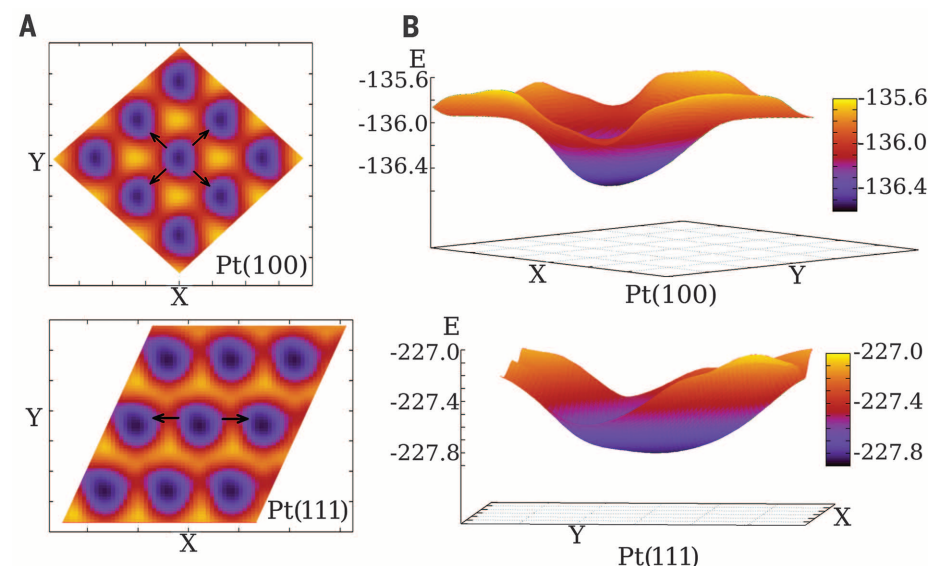


Fig. 4. The calculated potential energy of ethylamine molecule around Pt atoms on the (100) and (111) surfaces. The unit of the energy is eV. **(A)** The potential energy maps of an ethylamine molecule on Pt(100) and (111) surfaces. Arrows show the direction of the lowest energy barriers for the molecule to flip between two neighboring Pt atoms. **(B)** The calculated potential energy maps around one Pt atom on (100) and (111) surfaces. The energy barrier of a molecule to flip between two neighboring Pt atoms is 0.545 eV on the (100) surface and 0.298 eV on the (111) surface.

and 10^{-1} s on the (100) facet. Therefore, the ability of the surfactant ligands to move on the surface allows the (111) facet to grow, whereas the low mobility of the ligands on the (100) facet blocks its growth. However, this mechanism is only for large facets. For small nanocrystals, the ligand molecules can easily fan out to make room for platinum atoms to land (14). Therefore, all facets grow when the nanocrystal is small. The critical size of about 5 nm may vary with temperature or the type of ligand. Our proposed ligand mobility-controlled selective facet-arrested shape evolution may apply to other ligands and nanoparticle shapes.

REFERENCES AND NOTES

1. C. J. Murphy *et al.*, *J. Phys. Chem. B* **109**, 13857–13870 (2005).
2. Z. Tang, N. A. Kotov, M. Giersig, *Science* **297**, 237–240 (2002).
3. C. Burda, X. Chen, R. Narayanan, M. A. El-Sayed, *Chem. Rev.* **105**, 1025–1102 (2005).
4. M. Bruchez Jr., M. Moronne, P. Gin, S. Weiss, A. P. Alivisatos, *Science* **281**, 2013–2016 (1998).
5. M. C. Daniel, D. Astruc, *Chem. Rev.* **104**, 293–346 (2004).
6. R. Elghariani, J. J. Storchhoff, R. C. Mucic, R. L. Letsinger, C. A. Mirkin, *Science* **277**, 1078–1081 (1997).
7. P. L. Hansen *et al.*, *Science* **295**, 2053–2055 (2002).
8. E. Ringe, R. P. Van Duyne, L. D. Marks, *Nano Lett.* **11**, 3399–3403 (2011).
9. J. W. Gibbs, H. A. Bumstead, R. G. Van Name, W. R. Longley, *The Collected Works of J. Willard Gibbs* (Longmans, Green, City, 1902).
10. G. Wulff, *Z. Kristallogr. Mineral.* **34**, 449–530 (1901).
11. N. Tian, Z.-Y. Zhou, S.-G. Sun, Y. Ding, Z. L. Wang, *Science* **316**, 732–735 (2007).
12. Y. Xia, Y. Xiong, B. Lim, S. E. Skrabalak, *Angew. Chem. Int. Ed.* **48**, 60–103 (2009).
13. A. R. Tao, S. Habas, P. Yang, *Small* **4**, 310–325 (2008).
14. C. R. Bealing, W. J. Baumgardner, J. J. Choi, T. Hanrath, R. G. Hennig, *ACS Nano* **6**, 2118–2127 (2012).
15. M. J. Williamson, R. M. Tromp, P. M. Vereecken, R. Hull, F. M. Ross, *Nat. Mater.* **2**, 532–536 (2003).
16. H. Zheng *et al.*, *Science* **324**, 1309–1312 (2009).
17. J. E. Evans, K. L. Jungjohann, N. D. Browning, I. Arslan, *Nano Lett.* **11**, 2809–2813 (2011).
18. N. de Jonge, F. M. Ross, *Nat. Nanotechnol.* **6**, 695–704 (2011).
19. J. M. Yuk *et al.*, *Science* **336**, 61–64 (2012).
20. Y. Borodko *et al.*, *J. Phys. Chem. C* **117**, 26667–26674 (2013).
21. H.-G. Liao, L. Cui, S. Whitelam, H. Zheng, *Science* **336**, 1011–1014 (2012).

ACKNOWLEDGMENTS

We thank B. Sadtler for useful comments on the manuscript. Part of the in situ experiments was performed at Gatan, Incorporated using a Tecnai equipped with a K2-IS camera. We also used FEI Titan, Tecnai UT20, JOEL3010, and TEAM0.5 microscopes at the National Center for Electron Microscopy of Lawrence Berkeley National Laboratory, which is supported by the U.S. Department of Energy (DOE) Office of Basic Energy Sciences under contract no. DE-AC02-05CH11231. H.Z. was a residency faculty member of SinBeRise program of BEARS at University of California, Berkeley, during July 2013 to January 2014 and thanks the DOE Office of Science Early Career Research Program for support. The theoretical calculations were performed within the Organic/Inorganic Nanocomposite program in LBNL and funded by the Director, Office of Science, the Office of Basic Energy Sciences, Materials Sciences and Engineering Division of the U.S. Department of Energy (DOE) under contract DE-AC02-05CH11231. It used resources of the NERSC and Oak Ridge Leadership Computing supported by the Office of Science of the U.S. DOE under contract no. DE-AC02-05CH11231 and no. DE-AC05-00OR22725, respectively. The computational time at ORNL is allocated by Innovative and Novel Computational Impact on Theory and Experiment project.

SUPPLEMENTARY MATERIALS

www.sciencemag.org/content/345/6199/916/suppl/DC1

Materials and Methods

Supplementary Text

Figs. S1 to S20

References (22–32)

Movies S1 to S7

10 March 2014; accepted 3 July 2014

10.1126/science.1253149

GLACIERS

Attribution of global glacier mass loss to anthropogenic and natural causes

Ben Marzeion,^{1*} J. Graham Cogley,² Kristin Richter,¹ David Parkes¹

The ongoing global glacier retreat is affecting human societies by causing sea-level rise, changing seasonal water availability, and increasing geohazards. Melting glaciers are an icon of anthropogenic climate change. However, glacier response times are typically decades or longer, which implies that the present-day glacier retreat is a mixed response to past and current natural climate variability and current anthropogenic forcing. Here we show that only $25 \pm 35\%$ of the global glacier mass loss during the period from 1851 to 2010 is attributable to anthropogenic causes. Nevertheless, the anthropogenic signal is detectable with high confidence in glacier mass balance observations during 1991 to 2010, and the anthropogenic fraction of global glacier mass loss during that period has increased to $69 \pm 24\%$.

Although glaciers store less than 1% of global ice mass (1), their mass loss has been a major cause of sea-level rise during the 20th century (2). Glaciers are important regulators of the seasonal water cycle, providing meltwater during dry seasons in many regions of the world (3, 4). Glacier retreat often leads to the destabilization of mountain slopes and the formation of unstably dammed meltwater lakes, increasing the risk of rockslides and catastrophic outburst floods (5). The worldwide retreat of glaciers over the past decades has therefore had many impacts on human societies, which should increase over the 21st century because of continued mass losses (6–8).

Even though warming has accelerated over recent decades (9), glaciers have contributed to sea-level rise during most of the 20th century with relatively constant mass loss rates (2, 6, 10). The mass loss during the first decades of the 20th century was presumably governed by the loss of ice at low altitudes, when glaciers retreated from their 19th-century maxima at the end of the Little Ice Age (11). Because glacier extent responds to changes in the glacier mass balance (MB) with a lag of decades to centuries (12–14), glaciers provide an opportunity to directly perceive long-term climate change, unobscured by interannual variability. For this reason, images of retreating glaciers have become widely publicized illustrations of anthropogenic climate change. At the same time, the lagged response of glacier extents to climate changes complicates the attribution of the observed changes to any particular cause, because glacier mass change at any time is in part an ongoing adjustment of the glacier to previous climate change. The global retreat of glaciers observed today started around the middle of the 19th century, coinciding with the end of the Little Ice Age (10), when the anthropogenic forcing of the climate system was very weak as

compared to today (15). Given the response times of glaciers, it is therefore reasonable to hypothesize that glaciers at present are responding both to naturally caused climate change of past centuries and to the anthropogenic warming that has become stronger in recent decades. There is evidence that the recent mass loss of individual glaciers exceeds values expected from internal variability (16), and a rough estimate has been made of the influence of anthropogenic warming on global glacier mass loss (17), but the explicit attribution of observed changes of individual glaciers is also complicated by the dynamic response of glaciers' geometries to climate forcing, because internal variability alone may cause glacier changes of the magnitude observed since the end of the Little Ice Age (18).

Here we quantify the evidence for a causal link between anthropogenic climate forcing and observed glacier surface MBs, not of individual glaciers but of all the world's glaciers outside of Antarctica combined. We then attribute the global glacier retreat since 1851 to natural and anthropogenic causes. We use a model of global glacier evolution that treats the MB of each of the world's glaciers contained in the Randolph Glacier Inventory (RGI) (19, 20) individually, including a simple parametrization of ice dynamics leading to glacier hypsometry change (6). Forced by observed climate (21, 22), the glacier model has been independently validated against both annual surface MB observations (fig. S1) and observed, temporally accumulated volume changes of hundreds of glaciers (23), and has been used to reconstruct and project the global glacier mass change from 1851 to 2300 (6), based on climate reconstructions and projections from the Coupled Model Intercomparison Project phase 5 (CMIP5). See the supplementary materials for a comprehensive description of the model.

For each of 12 reconstructions of the global climate between 1851 and 2010, produced by general circulation models (GCMs) from the CMIP5 ensemble (see table S1 for the list of the experiments used), we reconstructed the area and volume of each glacier in 1851 (6). From this

¹Institute of Meteorology and Geophysics, University of Innsbruck, Austria. ²Department of Geography, Trent University, Peterborough, Canada.

*Corresponding author. E-mail: ben.marzeion@uibk.ac.at